communications biology

A Nature Portfolio journal

Article

https://doi.org/10.1038/s42003-025-08975-z

Characterization of the bone marrow architecture of multiple myeloma using spatial transcriptomics

Emma Muiños-Lopez[1,15] ✉, Ana Rosa Lopez-Perez[2,15], Laura Sudupe[3,15], Amaia Vilas-Zornoza[1], Sarai Sarvide[1], Purificacion Ripalda-Cemborain[1], Paula Aguirre-Ruiz[1], Patxi San Martin-Uriz[1], Marta Larrayoz[1,4], Laura Alvarez-Gigli[5], Marta Abengozar-Muela[5], Itziar Cenzano[1,3], Miguel Cócera[1,4], Javier Ruiz[6], Ignacio Sancho[6], Azari Bantan[3], Aleksandra Kurowska[3], Jin Ye[1], Phillip T. Newton[7,8], Bruno Paiva[1,4], Luis Esteban Tamariz-Amador[9], Juan R. Rodriguez-Madoz[1,4], Vincenzo Lagani[3,10,11,12], Jesper Tegner[3,12,13,14], Borja Saez[1], Jose Angel Martinez-Climent[1,4], Isabel A. Calvo[1,4,16] ✉, David Gomez-Cabrero[2,3,16] ✉ & Felipe Prosper[1,4,9,16] ✉

The bone marrow (BM) is a complex and compartmentalized tissue where spatial context plays a critical role in regulating cell behavior, signaling, and disease progression. To capture these dynamics, we apply spatial transcriptomics using the Visium Spatial Gene Expression platform on formalin-fixed paraffin-embedded (FFPE) BM sections from both healthy and Multiple Myeloma (MM) mouse models, as well as MM patient samples. Overcoming the technical challenges of working with mineralized long bone tissue, we develop a custom analytical framework integrating spatial and single-cell transcriptomic data to map cellular composition and interactions in situ. This approach enables the spatial characterization of transcriptionally heterogeneous malignant plasma cells (MM-PC) and their surrounding microenvironments. We identify spatially distinct gene programs linked to MM pathogenesis, including signatures of NETosis and IL-17 signalling, which are reduced in MM-PC–rich regions. Additionally, a transition gradient from effector to exhausted T cell phenotype is associated with increased remoteness from MM-PC. These spatial patterns are identified in FFPE BM biopsies from MM patients with varying tumor burdens. In summary, our study demonstrates both the capabilities and limitations of Visium technology in characterizing spatially regulated mechanisms underlying MM pathogenesis.

The bone marrow (BM) microenvironment is a specialized niche composed of stromal cells, blood vessels, immune cells, and extracellular matrix components, which play a crucial role in regulating hematopoietic stem cells (HSC). This environment supports cell growth, differentiation, and migration, impacting normal physiology and disease[1] The role of the BM microenvironment in developing and progressing Multiple Myeloma (MM), a B-cell malignancy characterized by the clonal expansion of abnormal plasma cells (PC) that infiltrate the BM[2], has been demonstrated[3–7]. Various mechanisms have been implicated in the expansion and growth of malignant PC. For example, the release of matrix metalloproteinases (MMPs) facilitates invasion into nearby tissues and metastasis, or the secretion of interleukins promotes myeloma cell growth or inhibits immune function[6,8]. Moreover, the induction of neutrophil extracellular traps (NETs) formation by neutrophils, or the impairment of T cell function, allows tumor expansion[7,9]. This evidence suggests that understanding the interaction between malignant cells and their BM microenvironment may contribute to the identification of novel therapeutic targets[10,11]. How these interactions are geographically distributed within the BM, the different relations between multiple myeloma PC (MM-PC) and other cellular components, and the impact that these interactions have on transcriptional programs is still unclear.

Advances in spatial-omics technologies have led to the development of diverse tools for analyzing spatially resolved biological information. These approaches can be broadly classified into sequencing-based methods, which decode spatial barcodes, and imaging-based methods, which visualize in situ mRNA. Additionally, these methods can be either targeted or untargeted,

A full list of affiliations appears at the end of the paper. ✉e-mail: emuinos@unav.es; icalvoa@unav.es; david.gomezcabrero@kaust.edu.sa; fprosper@unav.es

depending on the probes employed[12]. All the advances in spatial transcriptomics have provided the means to establish unbiased gene expression analysis with spatial context for different tissues, making these technologies complementary to single-cell methods that lack spatial resolution[13–15]. While tissues such as the heart or brain have been recently characterized through spatial transcriptomics, mineralized tissues such as BM possess a particular challenge[16–18]. These technical and biological challenges on bone tissues can limit the resolution and interpretability of the results: (1) the mineralized matrix necessitates decalcification, which can compromise RNA integrity and reduce the detection of transcripts; (2) BM samples—especially in pathological conditions like MM—often have low cellularity, particularly in non-hematopoietic compartments, which limits mRNA capture and leads to gene dropouts; (3) current platforms, such as Visium (10x Genomics), lack single-cell resolution, and (4) tissue processing artifacts (e.g., sectioning difficulties, folding, RNA diffusion) can introduce spatial bias and affect data quality; (5) moreover, the limited availability of matched single-cell datasets further hampers accurate cell-type annotation and transcript imputation[19].

Recent publications overcoming the spatial limitations of mineralized bone tissue[20–25] combined with integrating various predictive modeling packages for long bones[17], have led to significant advancements in studying BM regulation. However, the complexity of MM pathology and the use of healthy and malignant human samples continue to present considerable challenges[19,26].

In the current study, we used Visium Spatial Gene Expression (10x Genomics) technology on formalin-fixed paraffin-embedded (FFPE) bone femur sections as proof of concept to demonstrate its potential in MM research. To this end, we have spatially profiled our recently described $MI_{cγ1}$ MM and healthy mouse models[27] and human FFPE-BM samples from diseased and healthy individuals. This approach allowed us to explore the spatial organization of the BM in homeostasis and MM and interrogate transcriptional regulatory programs governing MM-PC and their surrounding microenvironment. Using a custom data-driven approach, we defined specific areas of MM-PC infiltration, facilitating the examination of the surrounding immune cells and their interactions based on the concentration of tumor cells. Our results highlighted MM-PC transcriptional heterogeneity between different malignant-cell-enriched areas, identified specific transcriptional programs associated with areas surrounding MM-PC and supported the distribution of subpopulations of T-cells. Some of the findings were confirmed in BM biopsies from MM patients with varying degrees of tumor PC infiltration. In summary, our study demonstrates that, despite its inherent limitations, Visium Spatial Gene Expression technology (10x Genomics) can effectively analyze FFPE BM samples, providing spatial insights into MM pathogenesis. Beyond its technical validation, our study introduces a novel framework for deciphering MM-PC interactions within the BM microenvironment, which could be instrumental in guiding future therapeutic strategies in MM.

Results

Spatial resolution of healthy bone marrow resident cell types

To elucidate the interactions between MM-PC and their surrounding microenvironment, we analyzed the spatial molecular landscape of cells within both healthy and malignant BM tissues. Building on previous reports[17], we first performed spatial transcriptomics of mouse femurs from a preclinical healthy mouse model[27] (YFPcγ1) using Visium Gene Expression (10X Genomics) (Fig. 1a and Supplementary Table 1). After preprocessing and quality control analysis, we detected a total of 1242 spots with an average of 3998 features and 14,118 counts per spot in the trabecular region of the bone (Fig. 1b and Supplementary Table 2). The cortical region presented a minimal number of counts, leading to its exclusion from the analysis. It is important to note that we observed a lower number of UMIs and features per spot compared to other non-decalcified tissues. Consequently, we applied a custom, data-driven thresholding approach for spot selection. Most of the subsequent analyses – detailed in Methods - were designed to yield robust results despite the low signal.

Since the BM is an unshaped tissue and each spatial transcriptomic spot captures a group of cells (between 3 and 10 cells)[28], we estimated the cell composition per spot. To this end, based on the literature, and considering the high sensitivity to parameter settings of deconvolution methods we first identified the most prevalent cell types in the BM[29]. Secondly, we estimated the cell proportion per spot by deconvolution analysis using single-cell RNA-seq (scRNA-seq) data as reference[30] (Fig. 1c and Supplementary Fig. 1a). Our spatial transcriptomics revealed neutrophils as the major cell type population, consistent with previous reports[29]. Next, we conducted a clustering analysis using the estimated cell proportion. We identified four groups of spots (CN1-CN4) (Fig. 1d). "Major cell type per spot" analysis (see Methods) was performed to determine the dominant cell type influence. Clusters 1 (CN1), 2 (CN2), and 3 (CN3) were characterized by a more significant proportion - when comparing between clusters - of DC, neutrophils, and T cells, respectively. Cluster 4 (CN4) exhibited the highest estimated percentage of neutrophils, while erythroblasts and B cells were reduced in this cluster. A positive spatial correlation between erythroblasts and B cells was observed, suggesting potential functional interactions between these two cell types (Fig. 1e), consistent with similar observations reported for mature cell populations[31]. In contrast, neutrophils presented negative correlations with erythroblasts, B cells, DC, and T cells, indicating a spatial distinction where neutrophils are less prevalent in regions where erythroblasts, B cells, DC, and T cells are more abundant. The distribution of different cell populations in healthy BM was visualized using Harris' Hematoxylin staining, which highlights cell nuclei in a deep blue purple. To specifically identify healthy PC, we performed immunostaining for Green Fluorescent Protein (GFP), using Diaminobenzidine (DAB) as the chromogen (Supplementary Fig. 1b).

The spatial distribution analysis of the different clusters revealed differences between the diaphysis (central area of the femur) and the epiphysis (extremes of the femur) (Fig. 1f). Notably, the spots in the healthy tissue's diaphysis were enriched in neutrophils. In contrast, the epiphysis of the femur showed an increased presence of erythroblasts (Fig. 1g and Supplementary Fig. 1c). These results were consistent with the expression patterns of *Retnlg* and *Fcer1g*, as well as *Tfrc* and *Cd36*, which are canonical markers of neutrophils and erythroblasts, respectively (Fig. 1h and Supplementary Fig. 1d).

To further validate the deconvolution analysis, we examined the distribution of significant cell populations by analyzing the expression of two representative markers per cell type (Supp Fig. 1d). Spatial enrichment of neutrophils in the diaphysis was confirmed by immunohistochemistry (IHC) for Ly-6G/Ly-6C (*Gr-1*) (Fig. 1i). The spatial localization of the remaining most BM cell types in healthy (YFP) mouse was similarly validated by IHC (Supp Fig. 1e). Taken together, we successfully describe the spatial configuration of the most prevalent cell type populations in healthy BM space in bone tissue.

Unraveling the transcriptional spatial profiling of multiple myeloma bone marrow

Following the same approach, we next aimed to characterize the structure of the BM under pathological conditions, and thus, we focused on MM as a case study of a tumor characterized by BM involvement. To that end, we used our recently described MM model ($MI_{cγ1}$), which recapitulates the principal clinical, genetic, and immunological characteristics of MYC and $IKK2^{NF\text{-}κB}$ -driven MM patients[27] (Fig. 2a). We spatially profiled mouse femurs from animals with different percentages of MM-PC infiltration (Supp Table 1 and Supplementary Fig. 2a), detecting a total of 1836 spatially defined spots with an average of 4914 features and 25,646 counts per spot (Supplementary Fig. 1b and Supplementary Table 2).

As myeloma samples are characterized by significant MM-PC infiltration, deconvolution of spatial spots was conducted using scBMReference (murine scRNA-seq dataset[30], used to annotate healthy BM, combined with our MM-PC scRNA-seq[32]) (Supplementary Fig. 2c, d). As expected, tumor PC were not detected in healthy BM samples (Fig. 2b, upper panel). In

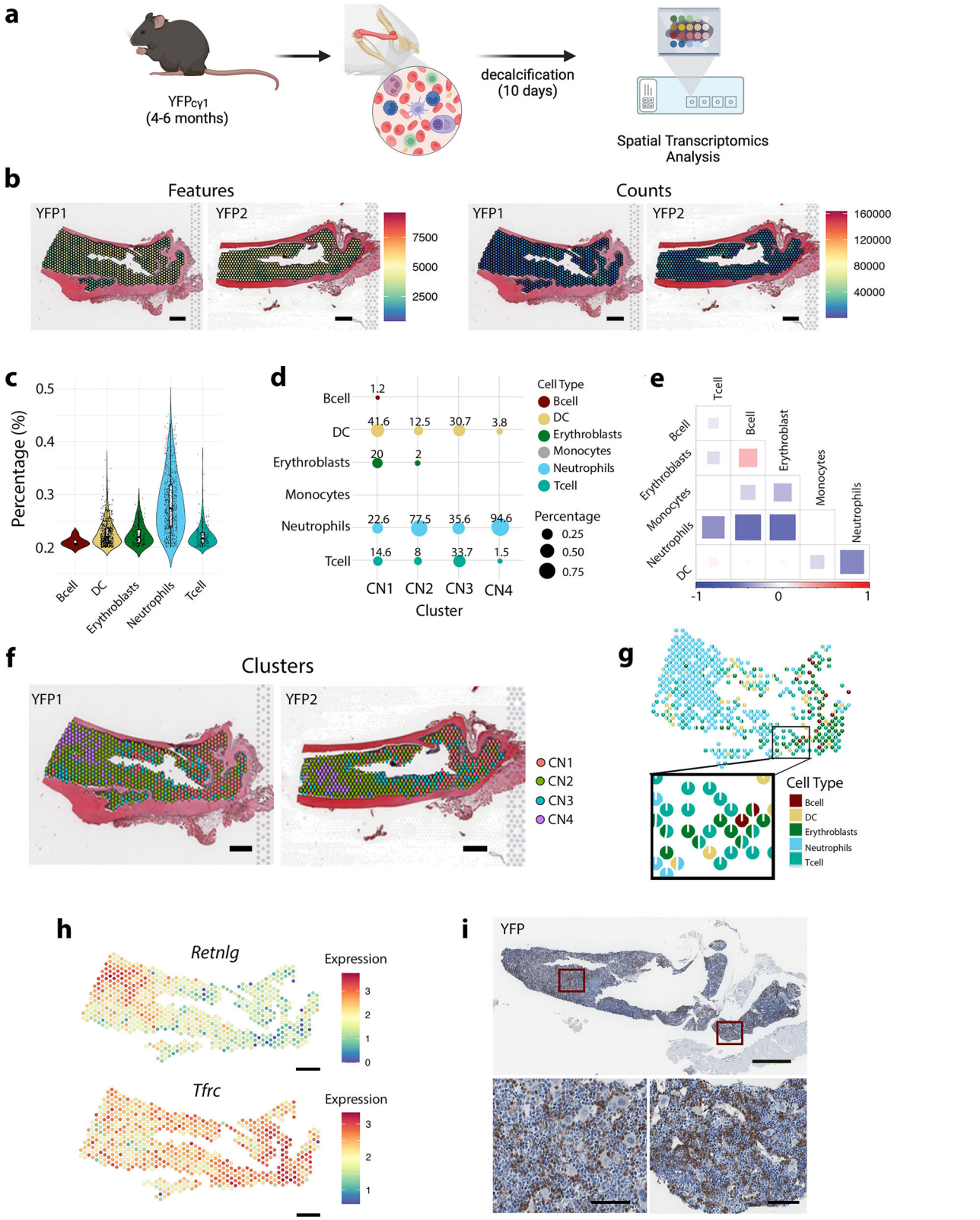

Fig. 1 | Spatial resolution of healthy bone marrow resident cell types. a Schematic representation of healthy control mouse (YFPcγ1), experimental workflow for bone tissue isolation and spatial transcriptomics analysis (created in BioRender, https://BioRender.com/u8jwp6c). **b** Quality control of the mice femur tissues, Features, and Counts in two samples from a control mouse model (YFP1 and YFP2)[16]. **c** Cell type proportions per spot derived from a deconvolution analysis using scRNA-seq data as a reference[19]. **d** Average of the most abundant cell types in the four identified clusters (CN1-CN4). **e** Correlation analysis of cell types based on spot distribution. **f** Spatial distribution of the four identified clusters. **g** Pie charts illustrating each cell type's proportion to each spot's transcriptomic signature in a control mouse model (YFP1). **h** *Retnlg* and *Tfrc* mouse gene expression, canonical markers of neutrophils and erythroblasts, respectively in a control mice femur sample (YFP1). **i** Immunohistochemistry (IHC) of Ly-6G/Ly-6C (*Gr-1*), a neutrophil marker, in control mice femur sample (YFP). Scales of 500 μm (**b**, **f**, and **h**), scales of 1000 μm (upper panel **i**) and 50 μm (bottom panels **i**).

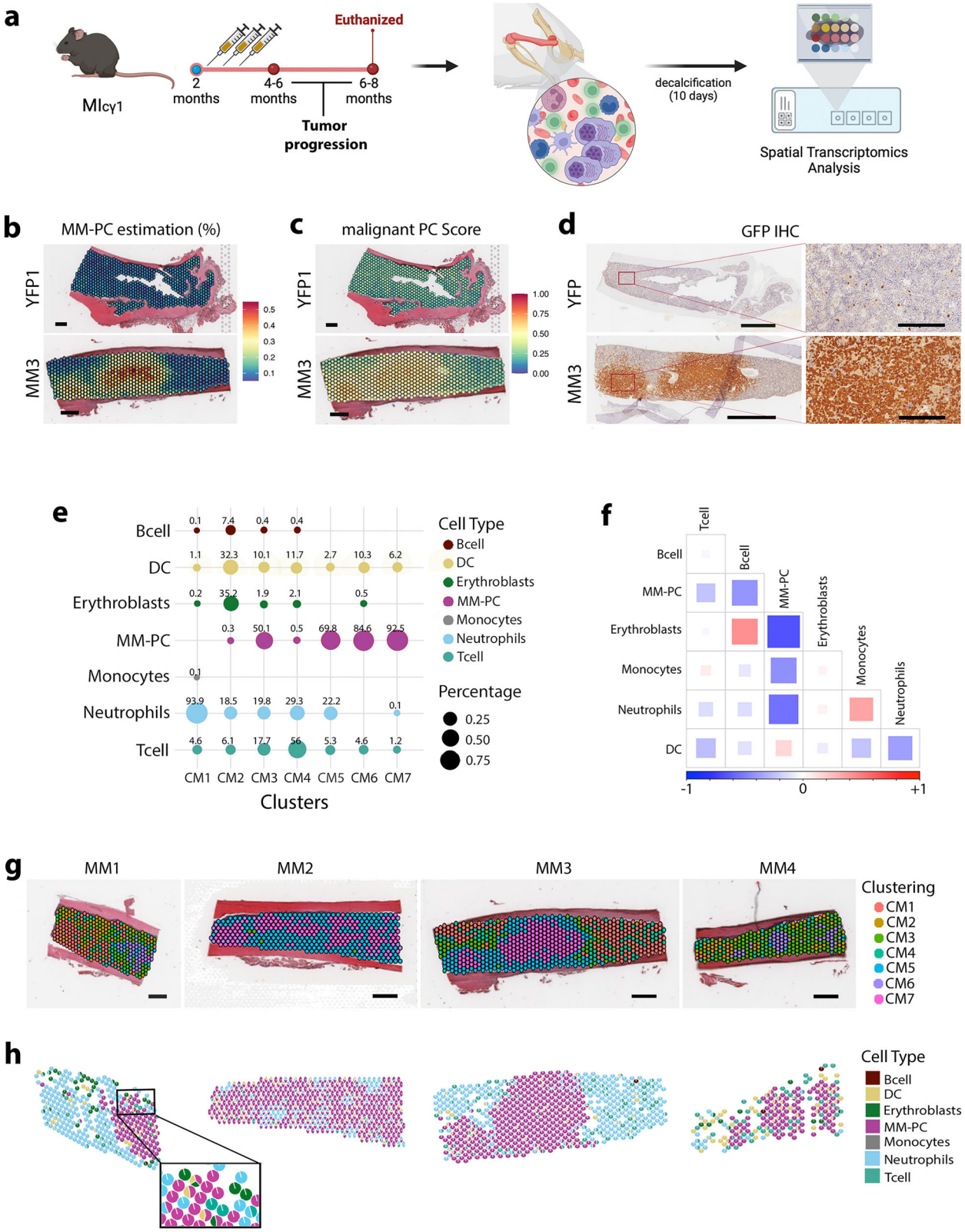

Fig. 2 | Unraveling the transcriptional spatial profiling of multiple myeloma bone marrow. a Schematic representation of MM mouse model (MIcγ1), experimental workflow for isolation bone tissue and conducting spatial transcriptomics (created in BioRender. https://BioRender.com/u8jwp6c). **b** Estimating malignant plasma cell (MM-PC) percentage per spot by deconvolution analysis using the scBMReference data set. **c** Enrichment score for malignant PC. **d** Green Fluorescent Protein (GFP) IHC of healthy YFPcγ1 and pathological MIcγ1 mice (MM3) femur tissues. **e** Average of the most abundant cell types in each of the seven identified malignant clusters (CM1-CM7). **f** Spot-based cell type correlation analysis between the different cell types. **g** Spatial distribution of the clusters identified in malignant samples. **h** Pie charts representing each cell type's contribution to each spot's transcriptomic signature. Scales of 500 µm (**b**, **c**, and **g**) and scales of 1000 µm (left panels **d**) and 100 µm (right panels **d**).

contrast, we observed a high proportion of the estimated percentage of MM-PC in several locations within each sample from MM mice (Fig. 2b, bottom panel, and Supplementary Fig. 3a). To further investigate, we compared the estimated MM-PC proportion per spot with a malignant PC gene-set score (Supplementary Table 3). This score is a unitless measure quantifying gene-set activity (also called a signature) per spot. We computed a malignant PC signature by comparing transcriptionally malignant PC with the cell types described at the single-cell level (Fig. 2c and Supplementary Fig. 3b). As expected, we detected a strong correlation between the MM-PC proportion and the enrichment score for malignant PC (Supplementary Fig. 3c). Based on this observation, we used cell proportions or signature scores in subsequent analyses, depending on the context. Notably, we observed heterogeneity in the spatial distribution of the estimated percentage of MM-PC across samples (Supplementary Fig. 3d). This result was verified by GFP expression analysis through IHC, as MM-PC in this model constitutively expresses GFP (Fig. 2d and Supplementary Fig. 13e).

We applied the same strategy used for healthy samples, i.e. estimated spot cell composition, cell types of prevalence and estimated the cell proportion, to samples with MM. Seven clusters (CM1- CM7) were identified (Supplementary Fig. 4). In clusters with a low proportion of MM-PC, clusters 1 (CM1) and 2 (CM2), we observed similar prevalence distributions to those in healthy samples, that is, the dominance of neutrophils or erythroblasts. However, the "Major cell type per spot" analysis indicated a steady proportion of T cells and DC in all the clusters, revealing the maximum malignant PC proportion from clusters 5 (CM5) to 7 (CM7) (Fig. 2e). When considering all spots in the BM area, we identified a negative correlation in cell proportion between MM-PC with erythroblasts, neutrophils, monocytes, and B cells, consistent with prior studies indicating that MM-PC displaced other hematopoietic populations in the BM of MM patients[33,34] (Fig. 2f). On the contrary, a positive correlation was seen with DC, also consistent with previous studies[35]. No specific pattern of spot distribution was identified, consistent with the described spatial clonal architecture and heterogeneous distribution of MM-PC[36] (Fig. 2g and Supplementary Fig. 4). However, identifying the different clusters allowed us to define the specific cell types surrounding the malignant PC (Fig. 2h), establishing the spatial relation between the different BM cell types and the MM-PC. To validate these cell types in MM samples, we examined the spatial expression of two representative markers (Supplementary Fig. 5) and confirmed their presence by IHC (Supplementary Fig. 6)

Overall, these results demonstrate the feasibility of applying spatial transcriptomics to fully mineralized murine diseased tissue, offering a comprehensive spatial overview of malignant PC heterogeneity in MM, yet limited to highly prevalent cell types.

Molecular characterization of plasma cell spatial heterogeneity

Looking into the spatial expression of several myeloma PC canonical markers, including *Sdc1, Tnfrsf17, Mzb1*, and *Xpb1*, we confirmed the presence of MM-PC groups in our malignant BM samples (Fig. 3a). We observed significant spatial heterogeneity in the expression of canonical PC markers, including *Mzb1*, *Xbp1* (Fig. 3a and Supplementary Fig. 7a), as well as MM-related markers (Supplementary Fig. 7b), within malignant-PC-enriched regions. To further characterize this spatial transcriptional heterogeneity of malignant PC, we performed a data-driven identification of areas with high concentrations of malignant PC using the healthy samples and the malignant PC score to establish criteria (Supplementary Fig. 8a). These criteria facilitated the identification of spots resembling healthy tissue, which we labeled "Rest" (areas without malignant PC). Subsequently, we classified the "non-Rest" spots into three categories -"Remote zone," "Border zone," and "Hotspot" - based on the density of MM-PC in each spot determined by the malignant PC signature (Fig. 3b) within each sample separately. Given the previously observed strong correlation between malignant PC score and MM-PC proportion, "Hotspot" indicated spatial areas with high malignant PC proportion. In contrast, the "Remote zone" signified areas with low proportions, and the "Border zone" encompassed the regions surrounding the hotspot. To further understand the heterogeneity of the MM-PC, we grouped the "Hotspots" based on their spatial positions to generate a graph, and using graph-based clustering for each sample (Supplementary Fig. 8b, c; see also Methods). This resulted in the identification of twelve transcriptionally distinct MM-PC groups (Pg1-Pg12) within the "Hotspot" areas among all the diseased samples (Fig. 3c). The areas and MM-PC groups identification were conducted separately for each sample to make the identified areas comparable despite the differences in MM-PC infiltration.

After identifying the multiple spatial MM-PC groups, we delved into their transcriptional profiles. First, we noted a distinct separation among certain Pg, highlighting the transcriptional heterogeneity of these groups within the BM when employing pseudo-bulk profiles computed for each Pg (Supplementary Fig. 8d). Secondly, we identified the top 1% of the most variable genes across the Pg1-Pg12 ($n = 194$) (Supplementary Fig. 8e and Supplementary Data 1). As a result, we observed specific expression patterns in the different MM-PC groups (Fig. 3d). Among the most variable genes, we found *B2m*, *Ptp4a3, Ly6k*, *Cyba, S100a6* and *Hsp90b1* (Fig. 3e and Supplementary Fig. 9). These genes have been implicated in numerous physiological processes and tumorigenesis, including the development of MM[37–41]. Still, some are expressed in the most prevalent cell type, neutrophils, such as *Ptp4a3* and *S100a6*. Over-representation analysis (ORA) on the highly variable genes identified pathways involved in major histocompatibility complex (MHC), immunoglobulin complex, cytoskeleton, vesicle, extracellular matrix, and NADPH oxidase complex (Fig. 3f and Supplementary Data 2). This analysis also highlighted the endoplasmic reticulum (ER)-related pathways corroborating the described role of ER and ER stress in MM's pathogenesis and drug resistance[42,43]. In summary, these findings provide additional support for the idea of transcriptional heterogeneity within MM, yet to be disentangled from the level of infiltration, and delineate distinct spatial expression patterns of both well-established and novel candidate genes associated with MM pathogenesis.

Spatial identification of transcriptional programs associated with multiple myeloma pathogenesis

Recognizing the BM microenvironment as a crucial contributor to MM pathogenesis and the role of T cells in the immune response to malignant PC infiltration, we analyzed different transcriptionally defined T cells according to their spatial relation to MM-PC[3,44,45]. Although T cells appeared to be evenly distributed across all spatial regions, independently of MM-PC prevalence, the score-based analysis of spatial transcriptomic signatures indicated the presence of effector T cells within the MM-PC Hotspot area (the spatial region with high concentrations of malignant PC), suggesting active immune aggression potentially targeting tumor cells (Fig. 4a–c, Supplementary Fig. 10ai, and Supplementary Data 3). Exhausted T cells[46] were predominant in the Border zone (areas surrounding the hotspots with less malignant PC proportion), representing a depleted immune microenvironment. This observation was further validated by IHC of MM-PC (GFP+), T cells (CD3+) and exhausted T cells by T-cell immunoglobulin 3 (TIM-3) (Supplementary Fig. 10b). This key T-cell exhaustion marker in our data, was noted for its role in T-cell exhaustion and suppression of innate immune responses in various malignancies[26].

Secondly, we conducted a data-driven approach to uncover additional microenvironmental signatures associated with MM. A differential expression analysis between the different areas identified 333 differentially expressed genes (DEG) between the Remote zone and Border zone (238 up- and 95 down-regulated) and 1710 DEG between the Border zone and Hotspot (1361 up- and 349 down-regulated) (Fig. 4d, Supplementary Fig. 11a, and Supplementary Data 4). Focusing on the 231 commonly up-regulated genes in these comparisons, we found an enrichment in many diverse biological processes highlighting leukocyte transendothelial migration and NETs formation, among others (Fig. 4e and Supplementary Data 4). Interestingly, when investigating the associated signatures, we observed a statistically significant decreased score for pathways related to interleukin-17 (IL-17) signaling, atherosclerosis, osteoclast differentiation, and NETosis within the Hotspots of tumor cells. These results suggested a

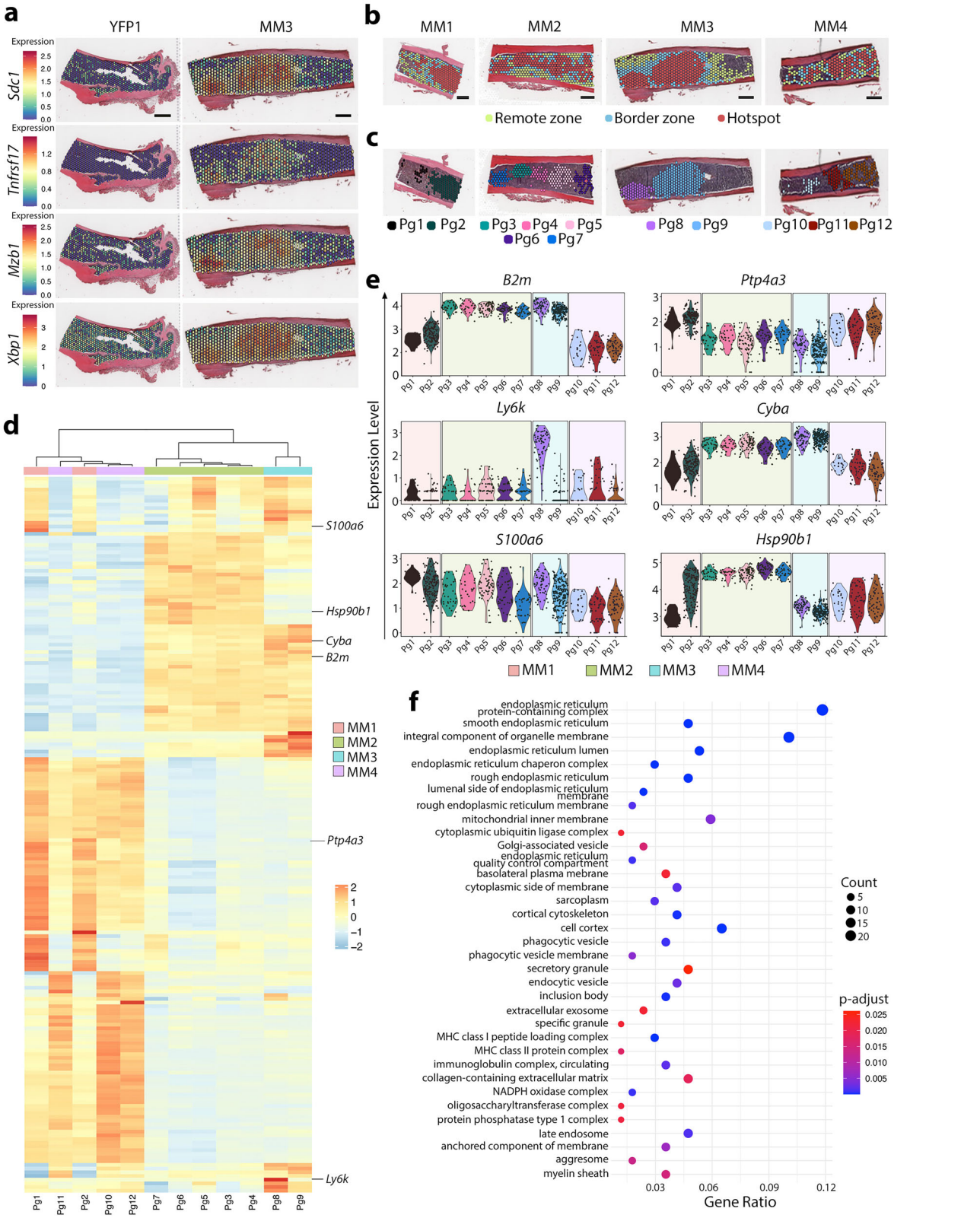

Fig. 3 | Molecular characterization of plasma cell spatial heterogeneity. a Spatial gene expression of pathological PC canonical markers. **b** Anatomical position of the identified areas (Remote zone, Border zone and Hotspot) based on their malignant PC signature. **c** Spatial distribution of the twelve identified MM-PC groups (Pg1-Pg12). **d** Heatmap of the top 1% most highly variable genes between the Pg groups shown in (**c**). **e** Violin plots of selected genes from (**d**). **f** Selected Gene Ontology (GO) terms derived from the over-representation analysis (ORA) of the most variable genes identified in (**d**) across Pg groups (the entire list is in Supplementary Data 2). Scales of 500 μm (**a** and **b**).

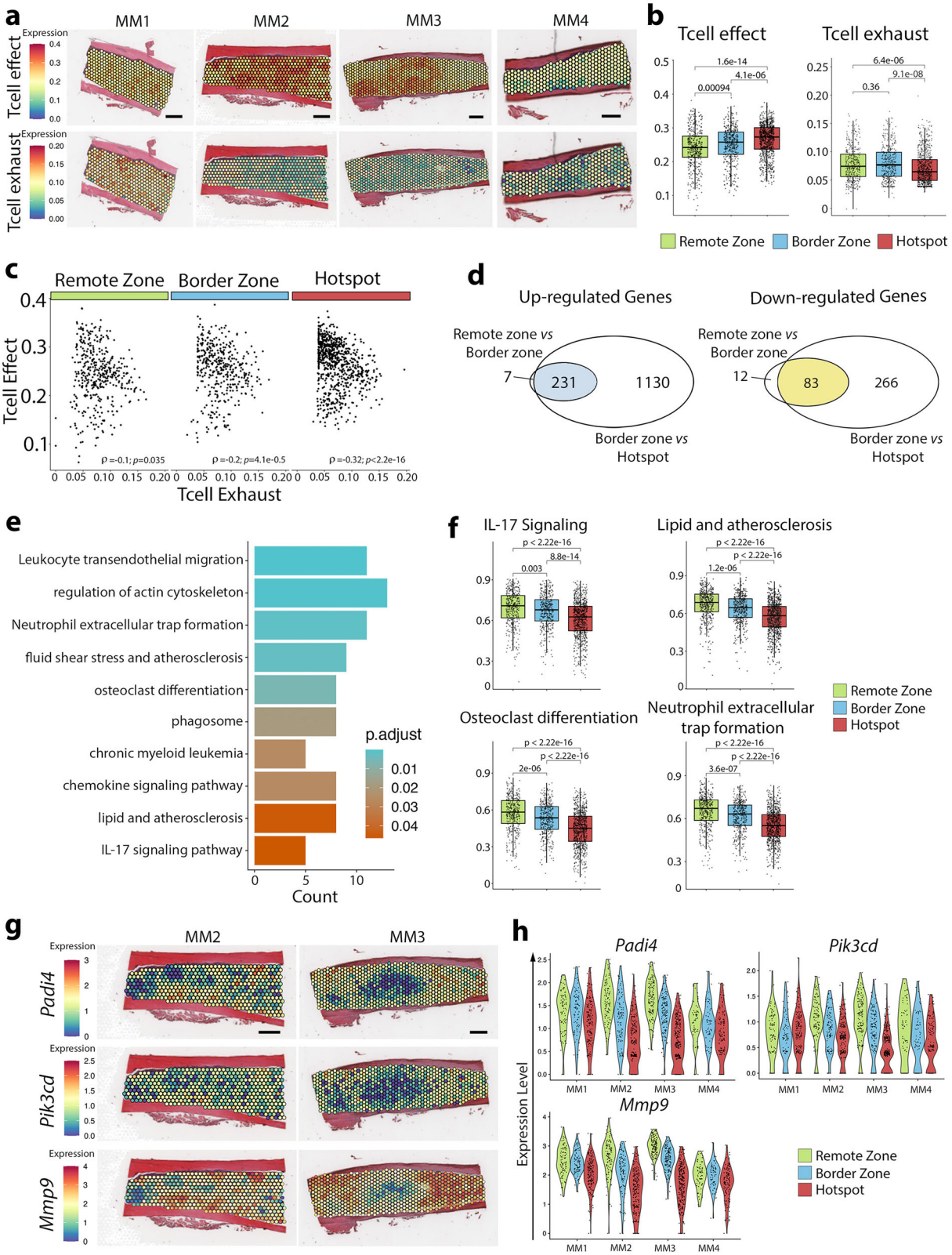

Fig. 4 | Spatial identification of transcriptional programs associated with multiple myeloma pathogenesis. a Spatial distribution of the T cell effector (upper panels) and T cell exhaustion (bottom panels) scores in the pathological samples. **b** Box plots illustrating the T cell effector and T cell exhaustion scores across different identified areas, with their corresponding *p*-values. **c** Correlation between the T cell effector and T cell exhaustion profiles in the three identified areas. **d** Venn diagram displaying the differentially expressed genes (DEG) between the different areas (Remote zone, Border zone, and Hotspot). **e** Bar plot indicating upregulated KEGG pathways from the 231 commonly upregulated genes identified in (**d**). **f** Box plots of selected KEGG pathways from (**e**). **g** Spatial distribution and **h** violin plots of *Padi4, Pik3cd*, and *Mmp9* genes expression level. Scales of 500 µm (**a** and **g**).

higher activity of these pathways in the MM-PC microenvironment compared to areas with tumor cells, specifically in the Remote zone (areas with low proportions of MM-PC) (Fig. 4f). Additionally, we observed similar trends in other pathways indicative of tissue remodeling post-MM development (Supplementary Fig. 11b). Notably, while these findings highlight apparent transcriptional differences between spatial regions, it is essential to consider that the distinct cellular composition of each region also influences these changes. As previously described, specific cell types are differentially distributed; for instance, neutrophils and MM-PC exhibit inverse spatial patterns (Fig. 2e), suggesting that the observed transcriptional changes may partially reflect these distinct cellular environments. To gain deeper insights into the molecular mechanisms driving the MM-PC microenvironment, we analyzed the spatial distribution of highly up-regulated genes in the Remote zone (Fig. 4g, h and Supplementary Fig. 11c–e). Moreover, we explored the involvement of innate immune processes by evaluating neutrophil infiltration and NETosis through IHC experiments (Supplementary Fig. 12). Specifically, we used GFP staining to identify MM-PC, *Gr-1* to detect neutrophils, and citrullinated histone H3 (*H3-cit*), as a marker of NETs[47]. These new IHC results confirmed our earlier spatial transcriptomic findings, showing that NETosis is predominantly localized in areas distant from MM-PC hotspots.

Altogether, these changes suggest that MM-PC infiltration influences the BM microenvironment´s response to tumor cells, leading to a progressive decline in inflammation, neutrophil activity, and matrix remodeling in regions with high MM-PC infiltration.

Spatial transcriptomic analysis of human bone marrow samples

To validate the findings obtained from mouse models, we conducted spatial transcriptomics on FFPE-BM samples from three healthy individuals and six MM patients (Supplementary Tables 4, 5 and Fig. 5a). First, we confirmed the presence of tumor regions in the samples by comparing Hematoxylin-Eosin staining (H&E) staining, malignant PC score, and the expression of key MM genes such as *CD81*, *XBP1*, and *TNFRSF17* (Fig. 5b–d, Supplementary Fig. 13a–c and Supplementary Table 6). We also demonstrated that these regions overlapped with CD38- or CD138-positive areas as determined by IHC (Fig. 5e and Supplementary Fig. 13d).

Next, using the MM-PC signature-derived scores, we categorized the spots of human MM samples into three distinct areas: "Remote Zone," "Border Zone," and "Hotspot" by adapting the analytical pipeline previously described for mice (Fig. 5f and Supplementary Fig. 14a–c). Regarding the MM-PC microenvironment, the human BM's enrichment of exhausted and effector T cells was less evident in humans than in mice (Fig. 5g and Supplementary Fig. 14d, e). While the effector T cells profile globally followed the same tendency between Hotspot (spatial areas with high tumor cell proportion) and surrounding areas (Border and Remote zone, areas with less proportion of MM-PC) as in mice, showing an increased score in Hotspot area, there was a slight tendency for an increase in the score of exhausted T cells also within areas with high proportion of malignant PC (Hotspot). These results suggest an increase in immune deregulation in MM patients. However, upon analyzing the transcriptional signatures associated with NETosis, IL-17 signaling, and related pathways, we noted a trend toward decreasing enrichment scores from the Remote zone to the Hotspot area. This pattern is reminiscent of our previous observations in the mouse model (Fig. 5h, i, and Supplementary Fig. 14f–h). Similarly, we observed comparable trends in other pathways potentially linked to tissue remodeling in the context of MM progression, which may reflect conserved features between human and murine BM microenvironments (Supplementary Fig. 15a, b). These data indicated that these pathways exhibit more significant activity in the Remote zones than in the Hotspot areas.

Taken together, these findings in human samples support our spatial transcriptomic approach and highlight its potential for clinical translation. Moreover, they enhance our understanding of the MM microenvironment's complexity while offering a novel framework for future therapeutic exploration.

Discussion

Recent spatial-omics studies have demonstrated the possibility of resolving the transcriptional spatial complexity, contributing to identifying novel mechanisms involved in tissue damage, cancer development, and inflammatory response. While this technique is readily applied to soft tissues, the requirement for bone decalcification -a process that typically degrades mRNA- has presented a significant challenge for mineralized tissues, such as BM simples[16,17,19,26]. Recent studies have demonstrated, for the first time, the potential of this technology to identify specific transcriptional pathways involved in the regulation of skeletal stem and progenitor cells in mice[17,48] and human[23–25,49]. Our study represents a significant technological advancement by enabling Visium to explore spatial cell organization in the BM across healthy and diseased states in mouse models and human subjects. Our work mainly validates current and partially extends the current understanding of malignant PC´s geographic and transcriptional heterogeneity and their associated microenvironment (Fig. 6).

The application of spatial technologies is endowed with significant technical challenges. Our initial efforts were focused on preserving RNA integrity during decalcification and using FFPE tissues, first optimized in mouse femurs and then in human samples. As current spatial technologies do not always have a single-cell resolution, our work using the 10X Visium CytAssyst-enabled workflow required the use of scRNA-seq data for deconvolution analysis. Other technologies based on targeted sequencing may provide single-cell or even sub-cellular resolution but have other limitations, such as not providing a genome-wide transcriptome analysis, allowing the profiling of significantly smaller regions, or inability to generate quality profiles in calcified tissues, among others.

Using Visium spatial transcriptomics technology on healthy mouse femur tissues, we confirmed previously known properties, such as the dominant role of neutrophils near blood vessels in healthy simples[50] and the correlations between different cell types pointing toward different surrounding areas within the BM microenvironment. Malignant PC canonical markers allowed us to identify distinct regions based on the proportion of MM-PC defined as Hotspot, Border, and Remote zones. In some cases, the expected concentric organization of zones (Hotspot surrounded by Border and Border surrounded by Remote zones) was not observed (e.g., in samples MM1 and MM4). This may reflect the technical limitations of the technology and the heterogeneous nature of the disease. Additionally, we characterized the spatially heterogeneous distribution of transcriptionally diverse malignant PC groups within areas of high tumor cell density. Interestingly, the observed differences in gene expression did not correlate with disease stage, as demonstrated in the MM1 and MM3 samples. Despite similar percentages of MM-PC infiltration, as determined by flow cytometry (Supplementary Table 1), the malignant PC populations exhibited distinct expression profiles of genes implicated in MM development and prognosis, including *B2m*, *Ly6k* and *Cyba*[51]. These variations may contribute to the heterogeneity observed in patient disease behavior. However, a more detailed and targeted analysis is required to elucidate the underlying mechanisms responsible for these differences.

An advantage of spatial transcriptomics is the possibility of adding spatial information to changes in transcriptional programs. As shown in our study, we characterized transcriptional programs associated with MM-PC density gradient involved in the pathogenesis of MM within the BM microenvironment. The spatial location of T effector cells was preferably around Hotspot areas, while the T exhausted phenotype was enriched in Remote and Border zones. These new findings in MM suggested potential similarities in the behavior of tumor microenvironment cells between solid tumors and MM[52]. We also identified the upregulation of several pathways in the malignant PC microenvironment indicative of its transcriptional remodeling in MM disease. The implications of IL-17 signaling, atherosclerosis, osteoclast differentiation, and the involvement of neutrophils through the NETosis mechanism contribute to the malignant PC microenvironment's spatial heterogeneity. Therefore, these results take a step further by highlighting the spatial role of tumor microenvironment cells in MM progression.

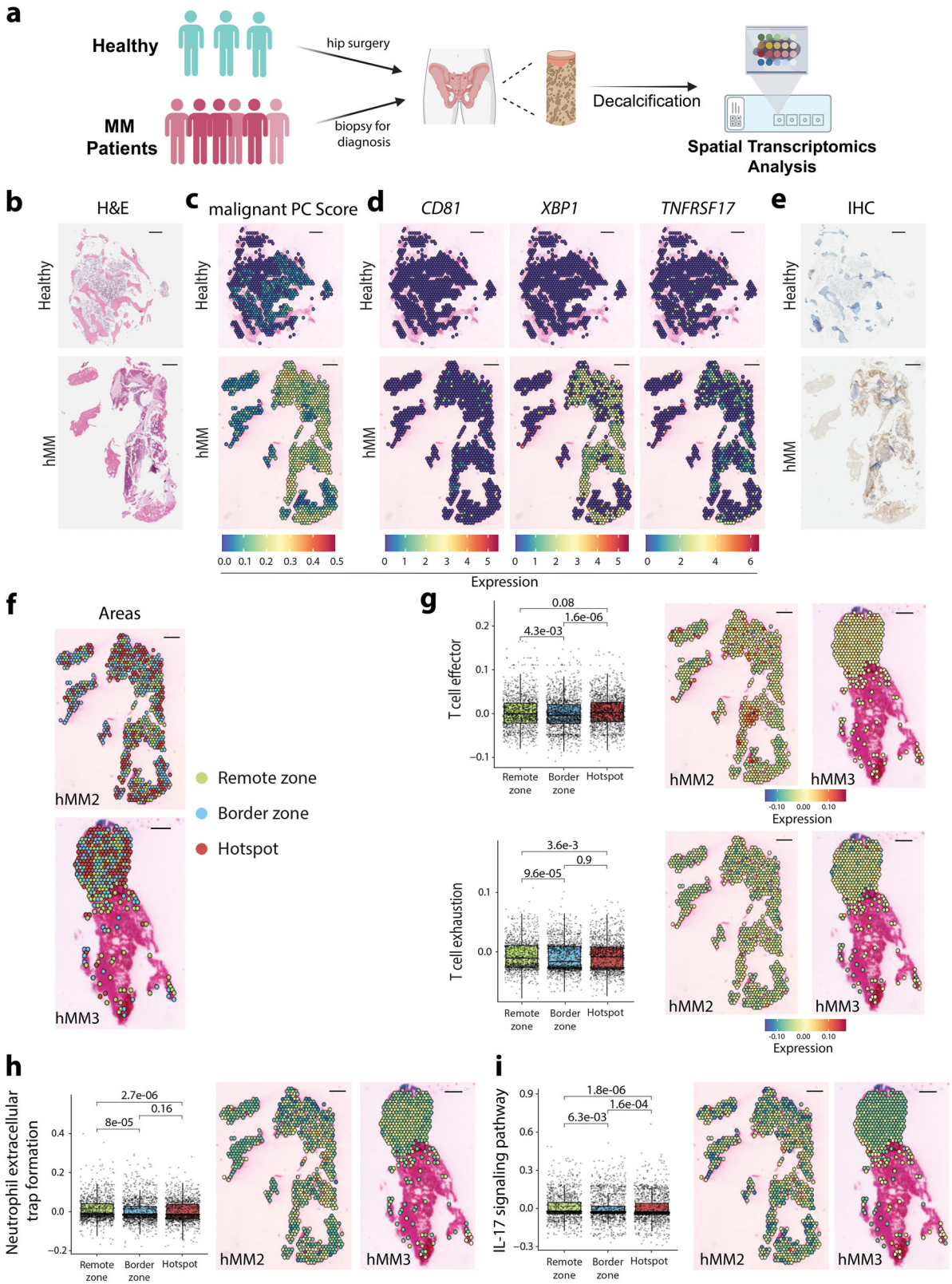

Fig. 5 | Spatial transcriptomic analysis of human bone marrow samples. **a** Experimental workflow for isolation and spatial transcriptomics analysis of healthy and MM human bone tissue samples (created in BioRender. https://BioRender.com/u8jwp6c). **b** Hematoxylin-Eosin staining (H&E) staining. **c** Spatial representation of the malignant PC enrichment score. **d** Spatial gene expression of human PC canonical markers. **e** CD138 (healthy) and CD38 (human malignant bone tissue (hMM)) IHC, of healthy (upper panels) and human malignant bone tissues (bottom panels). **f** Anatomical position of the identified areas (Remote zone, Border zone, and Hotspot) in two diseases samples, hMM2 and hMM3. **g** Box plots per area (mean of all the diseased samples) and spatial distribution of the T cell effector and T cell exhaustion scores. **h**, **i** Box plots per area (left panel) (mean of all the diseased samples) and spatial distribution of the scores associated with Neutrophil extracellular trap formation (NETs) (**h**) and with IL-17 signaling pathways (**i**) in two human malignant tissues (hMM2 and hMM3) (middle and right panel). Scales of 500 µm (**b**–**i**).

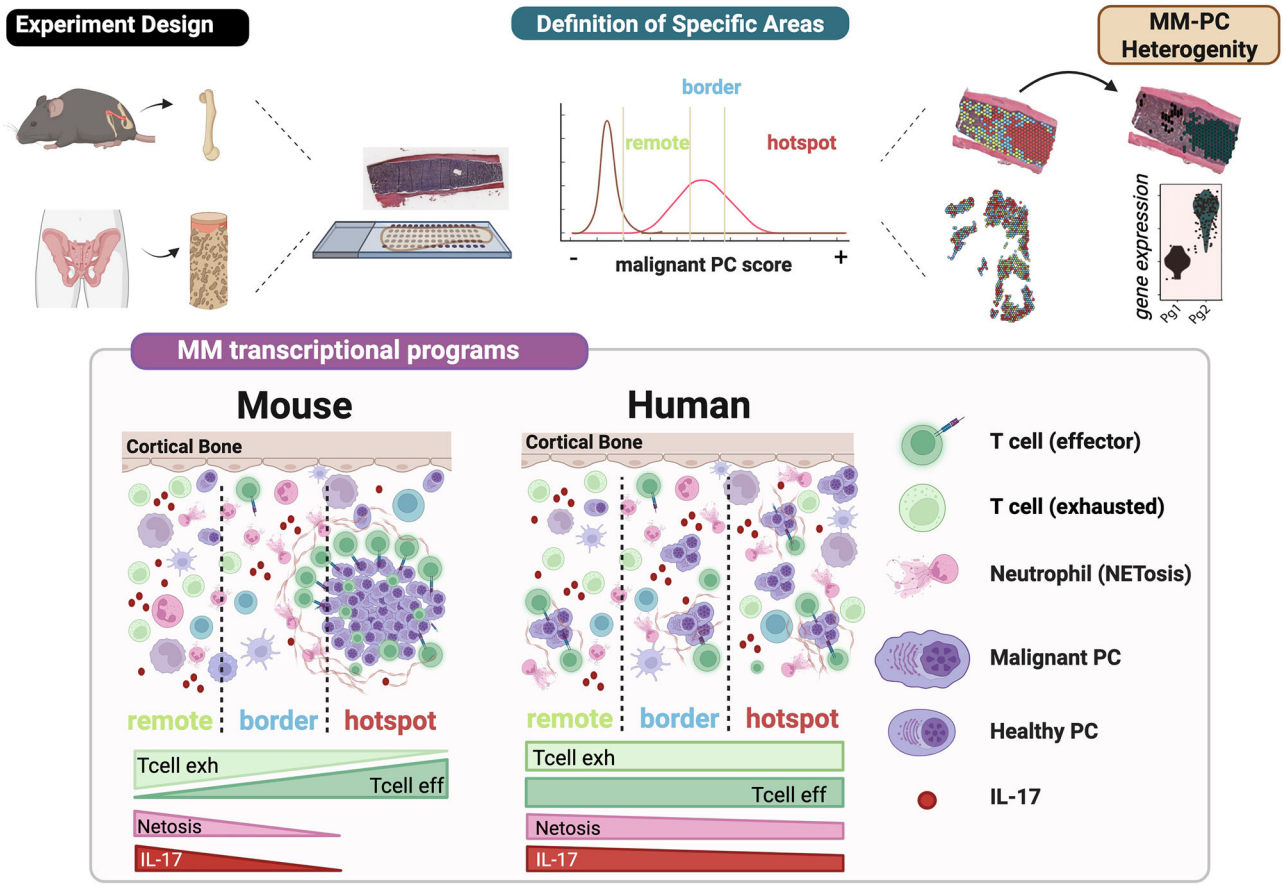

Fig. 6 | Summary figure. Created in BioRender, https://BioRender.com/u8jwp6c.

Our study was further validated in human samples by applying spatial transcriptomics to FFPE-BM biopsies from healthy and MM patients with various degrees of MM-PC infiltration. This validation underscores the reliability and relevance of our murine model's results. Like the findings in diseased mouse samples, we identified three distinct regions based on the spatial expression of malignant PC. The potential compromised structural integrity of human archive samples, along with the fact that trephine biopsies only represent a limited section of the bone, unlike mouse bone samples, may impact on the delineation of the different areas of MM-PC. This technical limitation may explain the differences in T cell behavior between humans and mice. However, our T cell human data, where we observed a modest but consistent trend toward increased exhaustion scores in regions with high MM-PC content (Hotspots), which was more aligned with findings from John et al.[26], who also reported checkpoint-expressing T cells—including TIM-3$^+$ cells—localizing near malignant cells. Additionally, the heterogeneity of human pathological samples—biopsies from four patients were obtained at diagnosis and two at relapse—may further contribute to discrepancies between human and murine data but again aligned with published related papers[53–56].

On the other hand, we observed similar transcriptional changes in the diseased BM between mice and humans, particularly in pathways related to NETosis and IL-17 signaling, among others. This consistency was evident as we moved from the Remote zone to the Hotspot region in human subjects. This further supports the idea that spatial organization influences the genetic activity underlying MM development and progression[9,57–59], regardless of the biopsy timing or disease stage.

While our investigation provided valuable insights into the spatial and transcriptional heterogeneity of myeloma, we acknowledge several limitations. Firstly, we analyzed a few samples, resulting in observational findings that deepen existing biological understanding but limit the potential for novel mechanistic insights. Among the limitations of the study is that, although a genomic aberration analysis using InferCNV did not yield any relevant insights, the quality and limited number of samples prevent us from robustly assessing the impact of genomic alterations. Second, as Visium is not a single-cell spatial technology, its resolution and reliance on single-cell data constrained our analysis – in our case from a different healthy reference -, primarily to large, prevalent cell types and gene-set score-based approaches. An example of such a limitation is that evaluating the importance of non-hematopoietic components is impossible because they represent less than 1% of the total BM. As a third associated limitation is that the methodology does not explicitly account for potential signal spillover between neighboring spots. Finally, it is relevant to mention that non-malignant cell proportions were inferred using a healthy reference derived from a separate dataset. Additionally, we could not fully assess the impact of low RNA quality in human samples, which may have been affected by the decalcification procedures used during sample processing.

Furthermore, while we examined tissues in three dimensions, our research only assessed one slide per sample, potentially missing critical spatial variations within the tissue. Lastly, MM is characterized by clonal immunoglobulin V(D)J signatures, originated during the normal process of B cell development, and driving an oncogenic immunoglobulin phenotype commonly present in premalignant conditions in similar percentages[60]. However, the current technology cannot conduct specialized analyses such as V(D)J recombination. Therefore, overcoming these limitations will be crucial for future mechanistic studies to advance our understanding of myeloma pathogenesis.

In conclusion, our findings demonstrate the feasibility of using Visium Spatial Gene Expression to investigate MM within the complex BM microenvironment. It also validates an FFPE-compatible protocol, which, when combined with a custom data-analysis framework, provides a

promising yet expandable approach for identifying spatial interactions between MM-PC and their BM niche.

Methods

Mice and human samples

For mouse studies, bone femur samples were obtained from control (YFPcγ1) and MM (MIcγ1)[27] derived, after CO_2 asphyxiation euthanasia, from mice females at age 4–12 months and submitted to Spatial transcriptomics interrogation. Animal experimentation was carried out following the European Communities Council Directive (2010/63/UE) and with the approval of the Ethical Committee of Animal Experimentation of the University of Navarra and the Health Department of the Navarra Government. For human studies, archived paraffined BM patient biopsies of six MM patients (47–78 years of age) and three fresh-collected elderly healthy controls were obtained from Pathology Department of Clínica Universidad de Navarra (CUN) and Hospital Universitario de Navarra, respectively, after written informed consent was achieved. The Research Ethics Committee of the University of Navarra approved the human sample collection and research conducted in this study. Personal data was kept confidential following the Organic Law 3/2018 on personal data protection and Spanish Law 14/2007 on Biomedical research. All collection samples are codified; only authorized personnel can correlate the patient's identity with the codes. No excluded samples were performed in this descriptive study.

Immunohistochemistry

Paraffin sections from mouse BM were immunostained using the following primary antibodies: goat anti-GFP (Novus Biologicals, NB100-1770, 1:4000, also recognizing YFP), rat anti-Gr1 (BioLegend, 108402, 1:1500), rabbit anti-CD3 (Invitrogen, MA1-90582, 1:200), rat anti-B220 (BD Pharmingen, 553083, 1:40000), rabbit anti-CD11c (Abcam, ab279799, 1:200), rat anti-Ter119 (BioLegend, 116204, 1:5000), rabbit anti H3-cit (H3-cit; Abcam, ab5103, 1:4000) and rabbit anti-TIM-3 (Cell Signaling, 83882, 1:400). Antigen retrieval with Tris-EDTA (pH 9) for 30 min at 95 °C was applied. In the case of rat and goat primary antibodies, sections were first incubated with rabbit anti-rat (Vector, BA-4001, 1:200) or rabbit anti-goat (Invitrogen, 31732, 1:200) secondary antibodies. Then, the EnVision system-HRP labeled polymer anti-rabbit (Dako, K4003) was used in all cases according to manufacturer instructions. Peroxidase activity was revealed using DAB+ (K3468, Dako). Finally, sections were lightly counterstained with Harris hematoxylin, dehydrated, and coverslipped. Sections from human BM cylinders were stained using an automated immunostaining platform (Discovery XT-ULTRA, Ventana-Roche) to reveal the presence of CD138 (B-A38) or CD38 (SP149) positive cells using the visualization system Omni-Map anti-rabbit conjugated to HRP. The reactions were developed with brown (ChromoMap DAB, Ventana, Roche) chromogen.

Flow cytometry analyses

Cell suspensions from BM (flushed from femurs with Dulbecco´s phosphate buffered saline-DPBS) were filtered through a 70-µm cell strainer (Falcon) and treated with ammonium-chloride-potassium-ACK lysis buffer to remove red blood cells. Then, the cells were washed in DPBS and filtered a second time before being labeled with antibodies for flow cytometry analysis. Mouse antibodies (Rat anti-mouse CD138-BD Pharmingen-Cat#553712; RRID: AB_394998 and APC anti-mouse/human CD45R/B220- BioLegend- Cat#103212; RRID: AB_312997) were used to detect tumor cell subpopulations (CD138+B220−GFP+). Data acquisition was performed in a FACS Canto II flow cytometer (BD Biosciences) and analyzed using FlowJo v10.7.1 software.

Spatial transcriptomics library preparation and sequencing

Bone femur mice samples were fixed in formol 4% (PanReac) for 24 h at room temperature (RT) and then decalcified with EDTA 0.25 M pH 6.95 (Invitrogen) for 10 days at RT with agitation. After decalcification, samples were washed in distilled water for 5 min and sequentially dehydrated in ethanol 70% (1 h), 80% (1 h), 96% (1 h), and 100% (overnight), followed by 4 h in xylol (Panreac). After dehydration, femurs were incubated in melted paraffin at 60 °C overnight to allow complete wax infiltration. The following day, samples were embedded in paraffin blocks for sectioning. Next, 5 µm tissue sections were mounted on microscopy slides, baked at 42 °C for 3 h, and dried in a desiccator at 37 °C overnight. For spatial transcriptomics assays, preparations were deparaffined, rehydrated, and H&E stained following 10X Genomics recommendations. Tissue imaging was performed using an Aperio CS2 Scanner (Leica Biosystems) at 20× magnification. Sections were destained and decrosslinked before library construction using Visium CytAssist Spatial Gene Expression for FFPE Mouse Transcriptome (10X Genomics). Briefly, a whole transcriptome panel consisting of probe pairs was hybridized with their target RNAs in the tissue sections. Neighboring probe pairs that had hybridized to RNA were then ligated. These ligated probes were then released through RNase treatment and tissue permeabilization and transferred to Visium slides containing spatially barcoded oligonucleotides using a CytAssist instrument (10X Genomics-v1). Probes were spatially labeled through extension, released from the slide, and pooled. Next, samples were indexed via PCR amplification. The resulting libraries were quantified with Qubit dsDNA HS Assay Kit, and their profile was examined using Agilent's HS D1000 ScreenTape Assay. Sequencing was carried out in an Illumina NextSeq2000 using paired-end, dual-index sequencing (Rd1: 28 cycles; i7: 10 cycles; i5: 10 cycles; Rd2: 50 cycles) at a minimum depth of 25000 reads per spot. As per the manufacturer's instructions, archived human FFPE-BM patients' biopsies mounted on microscopy slides were subjected to spatial transcriptomic analysis using Visium CytAssist Spatial Gene Expression for FFPE Human Transcriptome (10X Genomics-v2). The protocol workflow resembles the one described above, except tissue sections are directly mounted on Visium slides. Hence, upon the release of the probes that follow RNase treatment and tissue permeabilization, they directly diffuse onto the spatially barcoded oligonucleotides, precluding the need for a CytAssist instrument. In this case, the whole human transcriptome is covered with 3 probe pairs per targeted RNA.

Preprocessing and QC spatial transcriptomics data

Spatial transcriptomic data were demultiplexed and mapped using the SpaceRanger[61] software (v2.0.1). The Ensembl 105 genomes were used as reference (GRCh38 for humans and mm10 for mice samples). Filtered feature-barcode expression matrices obtained from SpaceRanger were used as initial input for the spatial transcriptomics analysis using Seurat[62] (v4.3.0.1) and STutility[63] (v1.1.1). Spots overlapping the cortical region of the bone were manually removed based on the H&E staining images using Cloupe (v6.0.0). For mouse samples, SCTransform[64] (v0.3.5) was used for normalization, using the regularized negative binomial regression, and for regressing out between-sample variations. Afterward, spots with less than 200 Unique Molecular Identifier (UMI) (also called counts), and 150 features (genes) were filtered out. Human samples were normalized with SCTransform[64] (v0.3.5), and spots corresponding to bone tissue were manually removed based on the H&E images using Cloupe (v6.0.0).

Single-cell RNA-seq data in mice

We downloaded a preprocessed murine single-cell dataset from https://apps.embl.de/nicheview/, published by Baccin et al.[30], for deconvolution analysis. We used the annotation contained in Baccin et al.[30]; we preselected six highly prevalent cell types for the reference (neutrophils, DC, T cells, erythroblast, B cells, and monocytes). Therefore, low prevalent cell types were filtered out or relabeled (e.g., all T cell subtypes into one); as a result, we generated a single cell set for the spot deconvolution of healthy murine BM. For the deconvolution of the spatial mouse MM samples, we included the malignant PC, MM-PC, obtained from Cenzano et al.[32]. The murine scRNA-seq dataset[30] used previously for healthy mice with the added MM-PC cell type new data set from malignant PC[32] were integrated using Harmony (v1.2.0) with default parameters (Supplementary Fig. 2c, d). We denote that integrated set as scBMReference.

Deconvolution analysis and hierarchical clustering in mice

Deconvolution analysis was performed in mice spatial transcriptomics data using scBMReference as the reference for CARD[65] (v1.0.0) with default parameters. Considering that estimating cell-type proportions is highly sensitive to the input parameters - including the number and quality of selected features, the number of cell types modeled, and their underlying proportions - we selected high-prevalent cells. The estimated cell-type percentage values derived from the deconvolution were used to cluster spots using the hierarchical clustering implementation in factoextra[66] (v1.0.7) with default parameters. The optimal number of clusters was determined by evaluating the consistency of marker gene expression profiles and employing the silhouette method; as a result, $k = 4$ and $k = 7$ was defined as the number of clusters in healthy and malignant samples, respectively. Each cluster's most abundant cell types were calculated by averaging the cell types contributing at least 20% to each spot signature. Correlation analyses were conducted using corrplot[67] (v0.92). Note that the prevalence analysis in Fig. 2b of MM-PC in healthy samples was conducted as a quality control, but they were not included in the clustering analysis. In dot-plots showing the average of the most abundant cell types and in the pie-chart-based spatial visualization, only cell types contributing at least 20% to each spot based on the deconvolution signature were considered. The proportion of these cell types was recalculated based on this filtering.

Spot labeling and plasma group identification in mice

We obtained the top marker genes (Supplementary Table 3) by comparing the transcriptome of the MM-PC versus the rest of the cell types included in our scBMReference, using the default Seurat pipeline. Then, we filtered out the genes that had no expression in our spatial transcriptomic datasets, both human and mouse samples. Malignant PC score was calculated using AUCell (v1.18.1), which computes the area under the curve for a given gene-set (a unitless measure) per spot. This score, also called signature, reflects the activity of a gene-set, in this case, the MM-PC marker genes. All the spots with a lower PC score than the value equivalent to the 90% percentile obtained in the healthy samples were removed from the next annotation steps and labeled as "Rest" (Supplementary Fig. 8a). Then, for each mice MM sample independently, the remaining spots were divided based on the malignant PC score using percentiles and labeled as "Remote zone" (malignant PC score < 25% percentile), "Border zone" (25% percentile < malignant PC score < 50% percentile) and "Hotspots" (malignant PC score > 50% percentile) (Fig. 3b). The labeling Hotspot-Border Zone-Remote zone denotes the expected concentric organization of these zones (with Hotspot surrounded by Border zone, and Border zone by Remote zone); however, this was not the case for all the spots in all mice samples. "Hotspot" spots were then grouped based on their spatial position using the igraph package (v1.5.1). Each spot was connected to its six nearest neighbors in the spatial configuration, reflecting their designed spatial distribution within the 10X Visium dataset. The silhouette score was employed to identify the appropriate resolution for modularity (Supplementary Fig. 8bi–c). As a result, "Hotspot" spots were grouped into twelve PC groups (Pg) (Fig. 3c).

Plasma group variability analysis in mice

Gene expression variability analysis within Pg was conducted using pseudo-bulk profiles. Reads from all the spots within each Pg were added; secondly, the resulting pseudo-count matrix was normalized using DESeq2 (v1.36.0). Standard error (SE) was calculated for each gene across all the Pg, and then genes were ranked based on this SE. The top 1% of genes were labeled highly variable (Supplementary Fig. 8e). Over-representation analysis (ORA) using GO was performed on the highly variable genes to identify the pathways associated with them using clusterProfiler (v4.4.4) with default parameters.

Differential analysis between regions

Differential analysis between the three areas ("Remote zone", "Border zone", and "Hotspot") was conducted with the FindMarkers function with default parameters from Seurat (v5.0.1) on the SCT Assay after merging data from the four MM mice samples. Genes were defined as significant if their adjusted p-values were <0.05. Subsequently, ORA was carried out on genes that were either up- (average log2 fold change >0) or down-regulated (average log2 fold change <0) for each of the comparisons ("Remote zone vs Border zone" and "Border zone vs Hotspot") using the Kyoto Encyclopedia of Genes and Genomes (KEGG) database. Moreover, the area under the curve was computed for several pathways using the AUCell (v1.18.1) using different gene sets of interest (Supplementary Table 3 and Supplementary Data 2 and Supplementary Data 4). Statistical comparisons of pathway scores across different zones were performed using the Wilcoxon statistics.

Spot labeling in human samples

As previously explained, spots were labeled based on each sample's malignant PC score within the MM-BM. Given the large variability in UMI counts between and within human samples, a preprocessing step was necessary. First, we divided each sample into bins based on the UMI counts, with 11 bins ranging from 0-500 to over 5000 UMIs (Supplementary Fig. 14a). Within each bin, we applied the per-sample analysis explained for mice (See Spot Labeling in mice). Briefly, spots with a malignant PC score below the 90% malignant PC score obtained from healthy human samples were labeled "Rest" and removed from the next annotation steps. Then, the remaining spots were further classified as "Remote zone" (malignant PC score < percentile 33), "Border zone" (percentile 33 < malignant PC score < percentile 66) or "Hotspot" (malignant PC score > percentile 66) (Supplementary Fig. 14b). Finally, the new labeling was assigned to the original Seurat Objects, ensuring the integrity of the spatial information. Even though in human samples there is no concentric annotation of these areas, we kept the labeling used in mice for consistency. Pathways scores were computed using the AUCell (v1.18.1) on raw counts for each sample (Supplementary Data 5). We corrected the scores using housekeeping genes (HSIAO_housekeeping_genes) to mitigate potential biases arising from technical differences by regressing out housekeeping-based signal. Statistical comparisons of pathway scores across different zones were conducted using Wilcoxon statistics, enabling robust assessments of pathway activity.

Statistics and reproducibility

In box plots, data are presented as mean ± standard error of the mean (SEM), with individual data points overlaid and in violin plots, individual data points are shown. All analyses were performed in R using the Wilcoxon for two-groups comparisons. A p-value < 0.05 was considered statistically significant.

For the mouse analyses, 2 healthy and 4 MM independent samples were included, and for the human analyses, 3 healthy and 5 MM independent samples were used. Each sample contains a number of spots ("n"), with the exact values provided in Supplementary Tables 2 and 5, respectively.

Reporting summary

Further information on research design is available in the Nature Portfolio Reporting Summary linked to this article.

Data availability

Mouse and human spatial raw and processed data have been deposited at GSE269875. Mouse scRNA-seq data used for deconvolution was obtained from Baccin et al.[30] (https://apps.embl.de/nicheview/).

Code availability

All original code has been deposited at https://github.com/lsudupe/spatialMM.

Received: 21 March 2025; Accepted: 30 September 2025;
Published online: 20 November 2025

References

1. Fröbel, J. et al. The hematopoietic bone marrow niche ecosystem. *Front. Cell Dev. Biol.* **9**, 705410 (2021).
2. Malard, F. et al. Multiple myeloma. *Nat. Rev. Dis. Prim.* **10**, 45 (2024).
3. García-Ortiz, A. et al. The role of tumor microenvironment in multiple myeloma development and progression. *Cancers* **13**, 217 (2021).
4. Chen, M. et al. Dynamic single-cell RNA-seq analysis reveals distinct tumor program associated with microenvironmental remodeling and drug sensitivity in multiple myeloma. *Cell Biosci.* **13**, 19 (2023).
5. de Jong, M. M. E. et al. The multiple myeloma microenvironment is defined by an inflammatory stromal cell landscape. *Nat. Immunol.* **22**, 769–780 (2021).
6. de Jong, M. M. E. et al. An IL-1β-driven neutrophil–stromal cell axis fosters a BAFF-rich protumor microenvironment in individuals with multiple myeloma. *Nat. Immunol.* **25**, 820–833 (2024).
7. Binder, A. F., Walker, C. J., Mark, T. M. & Baljevic, M. Impacting T-cell fitness in multiple myeloma: potential roles for selinexor and XPO1 inhibitors. *Front. Immunol*. **14**, 1275329 (2023).
8. Van Valckenborgh, E. et al. Multifunctional role of matrix metalloproteinases in multiple myeloma. *Am. J. Pathol.* **165**, 869–878 (2004).
9. Zhao, Z. et al. A neutrophil extracellular trap-related risk score predicts prognosis and characterizes the tumor microenvironment in multiple myeloma. *Sci. Rep.* **14**, 2264 (2024).
10. Garcia-Gomez, A. et al. Targeting aberrant DNA methylation in mesenchymal stromal cells as a treatment for myeloma bone disease. *Nat. Commun.* **12**, 421 (2021).
11. Schinke, C. & Weinhold, N. The immune microenvironment in multiple myeloma progression at a single-cell level. *HemaSphere* **7**, e894 (2023).
12. De Jonghe, J. et al. scTrends: A living review of commercial single-cell and spatial 'omic technologies. *Cell Genomics* **4**, 100723 (2024).
13. Quach, H. et al. Early human fetal lung atlas reveals the temporal dynamics of epithelial cell plasticity. *Nat. Commun.* **15**, 5898 (2024).
14. Fortelny, N. et al. JAK-STAT signaling maintains homeostasis in T cells and macrophages. *Nat. Immunol.* **25**, 847–859 (2024).
15. Roehrig, A. et al. Single-cell multiomics reveals the interplay of clonal evolution and cellular plasticity in hepatoblastoma. *Nat. Commun.* **15**, 3031 (2024).
16. Singh, V. M. et al. Analysis of the effect of various decalcification agents on the quantity and quality of nucleic acid (DNA and RNA) recovered from bone biopsies. *Ann. Diagn. Pathol.* **17**, 322–326 (2013).
17. Xiao, X. et al. Spatial transcriptomic interrogation of the murine bone marrow signaling landscape. *Bone Res.* **11**, 59 (2023).
18. Bandyopadhyay, S. et al. Mapping the cellular biogeography of human bone marrow niches using single-cell transcriptomics and proteomic imaging. *Cell* **187**, 3120–3140.e29 (2024).
19. Cooper, R. A., Thomas, E., Sozanska, A. M., Pescia, C. & Royston, D. J. Spatial transcriptomic approaches for characterising the bone marrow landscape: pitfalls and potential. *Leukemia* **39**, 291–295 (2025).
20. Wang, H. et al. Integrating spatial and single-cell transcriptomics to characterize mouse long bone fracture healing process. *Commun. Biol.* **8**, 887 (2025).
21. Tower, R. J. et al. Spatial transcriptomics reveals a role for sensory nerves in preserving cranial suture patency through modulation of BMP/TGF-β signaling. *Proc. Natl. Acad. Sci*. **118**, e2103087118 (2021).
22. Tower, R. J. et al. Spatial transcriptomics reveals metabolic changes underly age-dependent declines in digit regeneration. *Elife* **11**, e71542 (2022).
23. Lin, W. et al. Mapping the spatial atlas of the human bone tissue integrating spatial and single-cell transcriptomics. *Nucleic Acids Res*. **53**, gkae1298 (2025).
24. Gui, G. et al. Single-cell spatial transcriptomics reveals immunotherapy-driven bone marrow niche remodeling in AML. *Sci. Adv.* **11**, eadw4871 (2025).
25. Pelcovits, A. et al. 491 | spatial transcriptomics of follicular and marginal zone lymphomas identifies domains of CD8+ T cell recruitment and exclusion. *Hematol. Oncol.* **43**, e491–70096 (2025).
26. John, M. et al. Spatial transcriptomics reveals profound subclonal heterogeneity and T-cell dysfunction in extramedullary myeloma. *Blood* **144**, 2121–2135 (2024).
27. Larrayoz, M. et al. Preclinical models for prediction of immunotherapy outcomes and immune evasion mechanisms in genetically heterogeneous multiple myeloma. *Nat. Med.* **29**, 632–645 (2023).
28. Ståhl, P. L. et al. Visualization and analysis of gene expression in tissue sections by spatial transcriptomics. *Science* **353**, 78–82 (2016).
29. Hensel, J. A., Khattar, V., Ashton, R. & Ponnazhagan, S. Characterization of immune cell subtypes in three commonly used mouse strains reveals gender and strain-specific variations. *Lab. Investig.* **99**, 93–106 (2019).
30. Baccin, C. et al. Combined single-cell and spatial transcriptomics reveal the molecular, cellular and spatial bone marrow niche organization. *Nat. Cell Biol.* **22**, 38–48 (2020).
31. Lennon, C. S., Cao, H., Hall, A. M., Vickers, M. A. & Barker, R. N. The red blood cell as a novel regulator of human B-cell activation. *Immunology* **163**, 436–447 (2021).
32. Cenzano, I. et al. Transcriptional remodeling of the stromal and endothelial microenvironment in MGUS to multiple myeloma progression. *bioRxiv* **04**, 589777 (2024).
33. Schmidt-Hieber, M. et al. CD117 expression in gammopathies is associated with an altered maturation of the myeloid and lymphoid hematopoietic cell compartments and favorable disease features. *Haematologica* **96**, 328–332 (2011).
34. Bouchnita, A., Eymard, N., Moyo, T. K., Koury, M. J. & Volpert, V. Bone marrow infiltration by multiple myeloma causes anemia by reversible disruption of erythropoiesis. *Am. J. Hematol.* **91**, 371–378 (2016).
35. Leone, P. et al. Dendritic cells accumulate in the bone marrow of myeloma patients where they protect tumor plasma cells from CD8+ T-cell killing. *Blood* **126**, 1443–1451 (2015).
36. Rasche, L. et al. Spatial genomic heterogeneity in multiple myeloma revealed by multi-region sequencing. *Nat. Commun.* **8**, 268 (2017).
37. Papadea, C., Reimer, C. B. & Check, I. J. IgG subclass distribution in patients with multiple myeloma or with monoclonal gammopathy of undetermined significance. *Ann. Clin. Lab. Sci.* **19**, 27–37 (1989).
38. Zhang, L., Fok, J. H. L. & Davies, F. E. Heat shock proteins in multiple myeloma. *Oncotarget* **5**, 1132–1148 (2014).
39. Caillot, M., Dakik, H., Mazurier, F. & Sola, B. Targeting reactive oxygen species metabolism to induce myeloma cell death. *Cancers* **13**, 2411 (2021).
40. Tellier, J. & Nutt, S. L. Standing out from the crowd: how to identify plasma cells. *Eur. J. Immunol.* **47**, 1276–1279 (2017).
41. Liu, M. et al. S100 calcium binding protein family members associate with poor patient outcome and response to proteasome inhibition in multiple myeloma. *Front. Cell Dev. Biol*. **9**, 723016 (2021).
42. Wang, G., Fan, F., Sun, C. & Hu, Y. Looking into endoplasmic reticulum stress: the key to drug-resistance of multiple myeloma?. *Cancers* **14**, 5340 (2022).
43. Almanza, A. et al. Endoplasmic reticulum stress signalling – from basic mechanisms to clinical applications. *FEBS J.* **286**, 241–278 (2019).
44. Dolina, J. S., Van Braeckel-Budimir, N., Thomas, G. D. & Salek-Ardakani, S. CD8+ T cell exhaustion in cancer. *Front. Immunol*. **12**, 715234 (2021).
45. Joshua, D. E. et al. Treg and oligoclonal expansion of terminal effector CD8+ T cell as key players in multiple myeloma. *Front. Immunol*. **12**, 620596 (2021).

46. Bai, Y., Hu, M., Chen, Z., Wei, J. & Du, H. Single-cell transcriptome analysis reveals RGS1 as a new marker and promoting factor for T-cell exhaustion in multiple cancers. *Front. Immunol.* **12**, 767070 (2021).
47. Ciepiela, O., Małecka-Giełdowska, M. & Czyżewska, E. Neutrophil Extracellular Traps (NETs) and hypercoagulability in plasma cell dyscrasias—is this phenomenon worthy of exploration?. *J. Clin. Med.* **10**, 5243 (2021).
48. Bian, F. et al. Spatial transcriptomics reveals the requirement of ADGRG6 in maintaining chondrocyte homeostasis in mouse growth plates. *bioRxiv 2023* **09**, 558739 (2023).
49. Zheng, X. et al. A single-cell and spatially resolved atlas of human osteosarcomas. *J. Hematol. Oncol.* **17**, 71 (2024).
50. Maas, R. R. et al. The local microenvironment drives activation of neutrophils in human brain tumors. *Cell* **186**, 4546–4566.e27 (2023).
51. Wang, W. et al. Identification and validation of a novel RNA-binding protein-related gene-based prognostic model for multiple myeloma. *Front. Genet.* **12**, 665173 (2021).
52. Hsieh, W.-C. et al. Spatial multi-omics analyses of the tumor immune microenvironment. *J. Biomed. Sci.* **29**, 96 (2022).
53. Ninkovic, S., Purton, L. E., Harrison, S. J. & Quach, H. Multiplex immunohistochemistry elucidates increased distance between cytotoxic T cells and plasma cells in relapsed myeloma, and identifies Lag-3 as the most common checkpoint receptor on cytotoxic T cells of myeloma patients. *Haematologica* **109**, 1487–1500 (2023).
54. Fourcade, J. et al. Upregulation of Tim-3 and PD-1 expression is associated with tumor antigen–specific CD8+ T cell dysfunction in melanoma patients. *J. Exp. Med.* **207**, 2175–2186 (2010).
55. Gao, X. et al. TIM-3 expression characterizes regulatory T cells in tumor tissues and is associated with lung cancer progression. *PLoS One* **7**, e30676 (2012).
56. Das, M., Zhu, C. & Kuchroo, V. K. Tim-3 and its role in regulating anti-tumor immunity. *Immunol. Rev.* **276**, 97–111 (2017).
57. Lamanuzzi, A. et al. Thrombopoietin promotes angiogenesis and disease progression in patients with multiple myeloma. *Am. J. Pathol.* **191**, 748–758 (2021).
58. van Buul, J. D. & Hordijk, P. L. Signaling in leukocyte transendothelial migration. *Arterioscler. Thromb. Vasc. Biol.* **24**, 824–833 (2004).
59. Fu, J. et al. The checkpoint inhibitor PD-1H/VISTA controls osteoclast-mediated multiple myeloma bone disease. *Nat. Commun.* **14**, 4271 (2023).
60. Rustad, E. H. et al. Baseline identification of clonal V(D)J sequences for DNA-based minimal residual disease detection in multiple myeloma. *PLoS One* **14**, e0211600 (2019).
61. 10x Genomics Single Cell Analysis. SpaceRanger software (v2.0.1). https://github.com/10XGenomics/spaceranger (2023).
62. Stuart, T. et al. Comprehensive integration of single-cell data. *Cell* **177**, 1888–1902.e21 (2019).
63. Bergenstråhle, J., Larsson, L. & Lundeberg, J. Seamless integration of image and molecular analysis for spatial transcriptomics workflows. *BMC Genomics* **21**, 482 (2020).
64. Hafemeister, C. & Satija, R. Normalization and variance stabilization of single-cell RNA-seq data using regularized negative binomial regression. *Genome Biol.* **20**, 296 (2019).
65. Ma, Y. & Zhou, X. Spatially informed cell-type deconvolution for spatial transcriptomics. *Nat. Biotechnol.* **40**, 1349–1359 (2022).
66. Kassambara, A. & Mundt, F. Factoextra: Extract and Visualize the Results of Multivariate Data Analyses. R Package Version 1.0.7. https://CRAN.R-project.org/package=factoextra (2020).
67. Wei, T. & Simko, V. R Package "Corrplot": Visualization of a Correlation Matrix (2024).

Acknowledgements

This work was supported by the Instituto de Salud Carlos III and co-financed by ERDF A way of making Europe (PI20/01308, PI23/00516); CIBERONC (CB16/12/00489), RICORS TERAV (RD21/0017/0009); Departamento de Industria Gobierno de Navarra (AGATA 0011-1411-2020-000010/0011-1411-2020-000011) and Departamento de Salud Gobierno de Navarra (2024/04); the Cancer Research UK [C355/A26819]; FC AECC and AIRC under the Accelerator Award Program; The International Myeloma Foundation (Brian van Novis), The Paula and Rodger Riney Foundation and Fundación Alberto Palatchi to FP. The study was also supported by The Spanish Government through project PID2019-111192GA-I00 (MICINN) to DGC. IAC was supported by a Marie Curie grant (H2020- MSCA-IF-837491) from the European Commission. LS was supported by KAUST Discovery Doctoral Fellowship. We acknowledge the KAUST Baseline Awards, with DGC and LS supported by KAUST Baseline Award no. BAS/1/1093-01-01, and JT supported by KAUST Baseline Award no. BAS/1/1078-01-01.

We would like to thank the staff of the advanced genomic lab and the animal facility at CIMA Universidad de Navarra for their invaluable technical and intellectual assistance. We also acknowledge the Pathology Department of Clínica Universidad de Navarra (CUN), especially Jaione García Martínez and Vanessa Ocon Cruz, for the validation on the human samples, and Laura Guembe and Tania Lopez Martínez, for the validation of the mouse model, the Hospital Universitario de Navarra and the Biobank of the University of Navarra. We are particularly grateful to the patients and healthy donors who participated in this study.

Author contributions

L.S. and A.R.L.P. analyzed the spatial transcriptomic data. L.S., E.M.L., A.R.L.P. and I.A.C. interpreted the spatial transcriptomic data. E.M.L. achieved all the final figures. L.S. and I.A.C. wrote the paper; A.V., S.S., P.S.M. and P.A.R. performed the spatial transcriptomic experiments. P.R.C. performed the histologic analysis. M.L. and J.A.M.C. executed and ceded the animal model for this study. J.R. and I.S.G. provided the BM samples from healthy adult donors. L.A.G. and M.A. performed the histologic analysis and screening of the human samples. I.C. and M.C. assisted with the immunohistochemistry experiments. A.B., A.K., J.Y. and P.T.N. discussed the spatial analysis with L.S. and A.R.L.P. B.P. and L.E.T.A. contributed to the interpretation of the clinical data. J.R.R.M. and B.S. interpreted the T-cell-related biological data. D.G.C., with help from V.L. and J.T., supervised the computational work. E.M.L. conceived the research project. I.A.C., D.G.C. and. F.P. conceived and directed the research project. All authors actively participated in the discussions underlying this manuscript. L.S., E.M.L., A.R.L.P., I.A.C., D.G.C. and F.P. discussed the results and edited the final manuscript. All authors contributed to reading and approving the final manuscript.

Competing interests

The authors declare no competing interests. A patent on the know-how and experimental use of the MIcγ1 mouse models of MM has been licensed to MIMO Biosciences (application no. PCT/EP2023/071025).

Additional information

Supplementary information The online version contains supplementary material available at https://doi.org/10.1038/s42003-025-08975-z.

Correspondence and requests for materials should be addressed to Emma Muiños-Lopez, Isabel A. Calvo, David Gomez-Cabrero or Felipe Prosper.

Peer review information *Communications Biology* thanks Maximilian Merz and the other, anonymous, reviewer(s) for their contribution to the peer review of this work. Primary Handling Editor: Aylin Bircan.

[1]Hematology and Oncology Program, Centre for Applied Medical Research (CIMA), Instituto de Investigaciones Sanitarias de Navarra (IdiSNA), Cancer Center Clinica Universidad de Navarra (CCUN), Pamplona, Navarra, Spain. [2]Translational Bioinformatics Unit, Navarrabiomed, Universidad Pública de Navarra (UPNA), Pamplona, Navarra, Spain. [3]Bioscience Program, Biological and Environmental Sciences and Engineering Division (BESE), King Abdullah University of Science and Technology (KAUST), Thuwal, Saudi Arabia. [4]Centro de Investigacion Biomedica en Red de Cancer (CIBERONC), Madrid, Spain. [5]Departament of Pathology, Clinica Universidad de Navarra (CUN), Pamplona, Spain. [6]Hospital Universitario de Navarra, Instituto de Investigaciones Sanitarias de Navarra (IdiSNA), Pamplona, Spain. [7]Department of Women's and Children's Health, Karolinska Institutet, Stockholm, Sweden. [8]Astrid Lindgren Children's hospital, Stockholm, Sweden. [9]Hematology and Cell Therapy Department. Cancer Center Clinica Universidad de Navarra (CCUN), IdiSNA, Pamplona, Spain. [10]SDAIA-KAUST Center of Excellence in Data Science and Artificial Intelligence, Thuwal, Saudi Arabia. [11]Institute of Chemical Biology, Ilia State University, Tbilisi, Georgia. [12]Unit of Computational Medicine, Department of Medicine, Center for Molecular Medicine, Karolinska Institutet, Karolinska University Hospital, Stockholm, Sweden. [13]Computer, Electrical and Mathematical Sciences and Engineering Division, King Abdullah University of Science and Technology (KAUST), Thuwal, Saudi Arabia. [14]Science for Life Laboratory, Tomtebodavagen 23A, Solna, Sweden. [15]These authors contributed equally: Emma Muiños-Lopez, Ana Rosa Lopez-Perez, Laura Sudupe. [16]These authors jointly supervised this work. Isabel A. Calvo, David Gomez-Cabrero, Felipe Prosper. ✉e-mail: emuinos@unav.es; icalvoa@unav.es; david.gomezcabrero@kaust.edu.sa; fprosper@unav.es